formation mechanism of the hydrophilic cavities on the intracellular and extracellular sides. With the concomitant functional analyses, the present structural analysis suggested how the binding of either Ca^{2+} or H^+ induces the structural change (fig. S12): the gap between the TM2 and TM7 fixes the sliding of the gating bundle in the inward-facing, apo structure to prevent ion leakage across the membrane (*4*), while the binding of either Ca^{2+} or H^+ induces the gap closure, which enable the sliding motion of the gating bundle, as predicted from the NCX_Mj structure (*10*). Further discussion of the structural change mechanism may require the elucidation of the CAX_Af structure in the Ca^{2+} bound state.

References and Notes

1. E. Carafoli, Intracellular calcium homeostasis. *Annu. Rev. Biochem.* **56**, 395 (1987). doi:10.1146/annurev.bi.56.070187.002143 Medline
2. M. J. Berridge, M. D. Bootman, H. L. Roderick, Calcium signalling: dynamics, homeostasis and remodelling. *Nat. Rev. Mol. Cell Biol.* **4**, 517 (2003). doi:10.1038/nrm1155 Medline
3. D. E. Clapham, Calcium signaling. *Cell* **131**, 1047 (2007). doi:10.1016/j.cell.2007.11.028 Medline
4. M. P. Blaustein, W. J. Lederer, Sodium/calcium exchange: its physiological implications. *Physiol. Rev.* **79**, 763 (1999). Medline
5. J. Lytton, Na^+/Ca^{2+} exchangers: three mammalian gene families control Ca^{2+} transport. *Biochem. J.* **406**, 365 (2007). doi:10.1042/BJ20070619 Medline
6. X. Cai, J. Lytton, The cation/$Ca^{(2+)}$ exchanger superfamily: phylogenetic analysis and structural implications. *Mol. Biol. Evol.* **21**, 1692 (2004). doi:10.1093/molbev/msh177 Medline
7. L. Emery, S. Whelan, K. D. Hirschi, J. K. Pittman, Protein Phylogenetic Analysis of $Ca^{(2+)}$/cation Antiporters and Insights into their Evolution in Plants. *Front. Plant Sci.* **3**, 1 (2012). doi:10.3389/fpls.2012.00001 Medline
8. E. M. Schwarz, S. Benzer, Calx, a Na-Ca exchanger gene of Drosophila melanogaster. *Proc. Natl. Acad. Sci. U.S.A.* **94**, 10249 (1997). doi:10.1073/pnas.94.19.10249 Medline
9. K. D. Philipson, D. A. Nicoll, Sodium-calcium exchange: a molecular perspective. *Annu. Rev. Physiol.* **62**, 111 (2000). doi:10.1146/annurev.physiol.62.1.111 Medline
10. J. Liao *et al.*, Structural insight into the ion-exchange mechanism of the sodium/calcium exchanger. *Science* **335**, 686 (2012). doi:10.1126/science.1215759 Medline
11. O. Boudker, G. Verdon, Structural perspectives on secondary active transporters. *Trends Pharmacol. Sci.* **31**, 418 (2010). doi:10.1016/j.tips.2010.06.004 Medline
12. M. Caffrey, V. Cherezov, Crystallizing membrane proteins using lipidic mesophases. *Nat. Protoc.* **4**, 706 (2009). doi:10.1038/nprot.2009.31 Medline
13. M. Petrek *et al.*, CAVER: a new tool to explore routes from protein clefts, pockets and cavities. *BMC Bioinformatics* **7**, 316 (2006). doi:10.1186/1471-2105-7-316 Medline
14. P. S. Chae *et al.*, Maltose-neopentyl glycol (MNG) amphiphiles for solubilization, stabilization and crystallization of membrane proteins. *Nat. Methods* **7**, 1003 (2010). doi:10.1038/nmeth.1526 Medline
15. L. Goldschmidt, D. R. Cooper, Z. S. Derewenda, D. Eisenberg, Toward rational protein crystallization: A Web server for the design of crystallizable protein variants. *Protein Sci.* **16**, 1569 (2007). doi:10.1110/ps.072914007 Medline
16. T. R. Schneider, G. M. Sheldrick, Substructure solution with SHELXD. *Acta Crystallogr. D Biol. Crystallogr.* **58**, 1772 (2002). doi:10.1107/S0907444902011678 Medline
17. E. de La Fortelle, G. Bricogne, Maximum-likelihood heavy-atom parameter refinement for multiple isomorphous replacement and multiwavelength anomalous diffraction methods. *Methods Enzymol.* **276**, 472 (1997). doi:10.1016/S0076-6879(97)76073-7
18. J. P. Abrahams, A. G. Leslie, Methods used in the structure determination of bovine mitochondrial F1 ATPase. *Acta Crystallogr. D Biol. Crystallogr.* **52**, 30 (1996). doi:10.1107/S0907444995008754 Medline
19. P. Emsley, B. Lohkamp, W. G. Scott, K. Cowtan, Features and development of Coot. *Acta Crystallogr. D Biol. Crystallogr.* **66**, 486 (2010). doi:10.1107/S0907444910007493 Medline
20. P. D. Adams *et al.*, PHENIX: a comprehensive Python-based system for macromolecular structure solution. *Acta Crystallogr. D Biol. Crystallogr.* **66**, 213 (2010). doi:10.1107/S0907444909052925 Medline
21. L. Leive, Studies on the permeability change produced in coliform bacteria by ethylenediaminetetraacetate. *J. Biol. Chem.* **243**, 2373 (1968). Medline
22. B. Martinac, M. Buechner, A. H. Delcour, J. Adler, C. Kung, Pressure-sensitive ion channel in Escherichia coli. *Proc. Natl. Acad. Sci. U.S.A.* **84**, 2297 (1987). doi:10.1073/pnas.84.8.2297 Medline
23. D. M. Bers, C. W. Patton, R. Nuccitelli, A practical guide to the preparation of $Ca^{(2+)}$ buffers. *Methods Cell Biol.* **99**, 1 (2010). doi:10.1016/B978-0-12-374841-6.00001-3 Medline
24. T. J. Dolinsky *et al.*, PDB2PQR: expanding and upgrading automated preparation of biomolecular structures for molecular simulations. *Nucleic Acids Res.* **35**, (Web Server), W522 (2007). doi:10.1093/nar/gkm276 Medline

Acknowledgements: We thank H. Nishimasu and M. Hattori for useful discussions and critical comments on the manuscript; A. Kurabayashi for technical assistance; the beam-line staffs at BL32XU and BL41XU of SPring-8 for assistance in data collection; and the RIKEN BioResource Center (Ibaraki, Japan) for providing the *Archaeoglobus fulgidus* genomic DNA. The diffraction experiments were performed at SPring-8 BL32XU and BL41XU (proposals 2012A1093, 2012A1201, and 2012A1087), and with the approval of RIKEN. Part of this work was performed with the support of the Radioisotope Center, The University of Tokyo. This work was supported by the Japan Society for the Promotion of Science (JSPS) through its "Funding Program for World-Leading Innovative R&D on Science and Technology (FIRST program)" to O.N., by the Core Research for Evolutional Science and Technology (CREST) Program 'The Creation of Basic Medical Technologies to Clarify and Control the Mechanisms Underlying Chronic Inflammation' of Japan Science and Technology Agency (JST) to O.N., by a grant for HPCI STRATEGIC PROGRAM Computational Life Science and Application in Drug Discovery and Medical Development by MEXT to R.I., by a Grant-in-Aid for Scientific Research on Innovative Areas (23136517) from Ministry of Education, Culture, Sports, Science and Technology (MEXT) to S.K., by a Grant-in-Aid for Scientific Research (C) (23590319) from JSPS to T.I., and by a Grant-in-Aid for Scientific Research (S) (24227004) and a Grant-in-Aid for Young Scientists (A) (22687007) from the MEXT to O.N. and R.I., respectively. T.N. expressed and purified CAX_Af for crystallization, collected the diffraction data, solved the structures and performed functional analyses in liposomes. N.F. screened CaCA genes and identified CAX_Af. S.K. and T.I. performed transport assays in *E. coli* cells. A.D.M. performed transport assays in *E. coli* spheloplasts. G.K. made mutants. K.H. assisted with data collection. S.O. supported crystallization. N.D. analyzed the purified protein by mass spectrometry. T.N., R.I., and O.N. wrote the manuscript. R.I. and O.N. directed and supervised all of the research.

Supplementary Materials

www.sciencemag.org/cgi/content/full/science.1239002/DC1
Materials and Methods
Supplementary Text
Figs. S1 to S14
Tables S1 to S2
References (*14–24*)
Movie S1

10 April 2013; accepted 15 May 2013
Published online 23 May 2013
10.1126/science.1239002

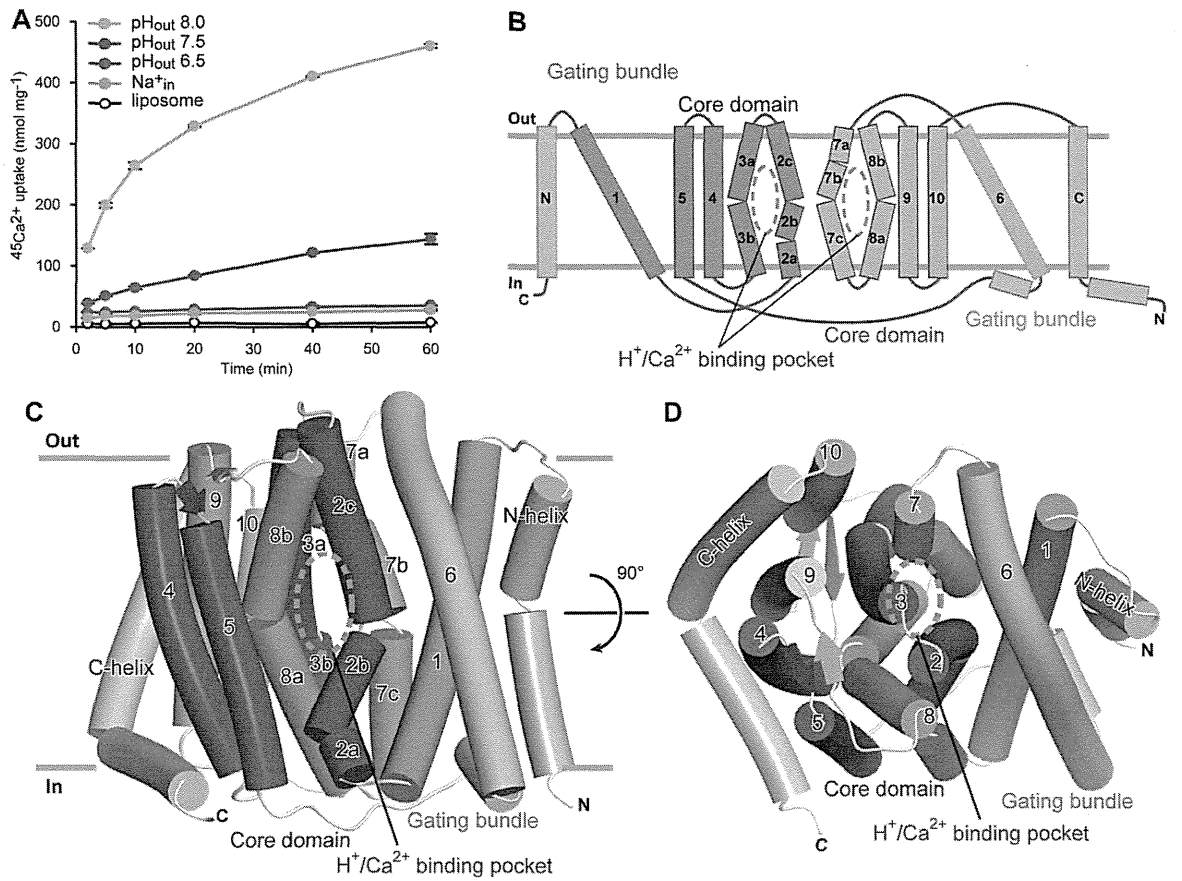

Fig. 1. The overall structure and function of CAX_Af. (**A**) Time courses of $^{45}Ca^{2+}$ uptake by liposome-reconstituted CAX_Af at different pH values. (**B**) Schematic representation of the CAX_Af topology. The core domain and the gating bundle are colored blue and orange, respectively. The additional helices are gray. The H^+/Ca^{2+} binding pockets are indicated by green dotted circles. (**C** and **D**) Structure of CAX_Af (Mol A) as viewed from the membrane plane (C) or the extracellular side (D). The color coding is the same as in (B).

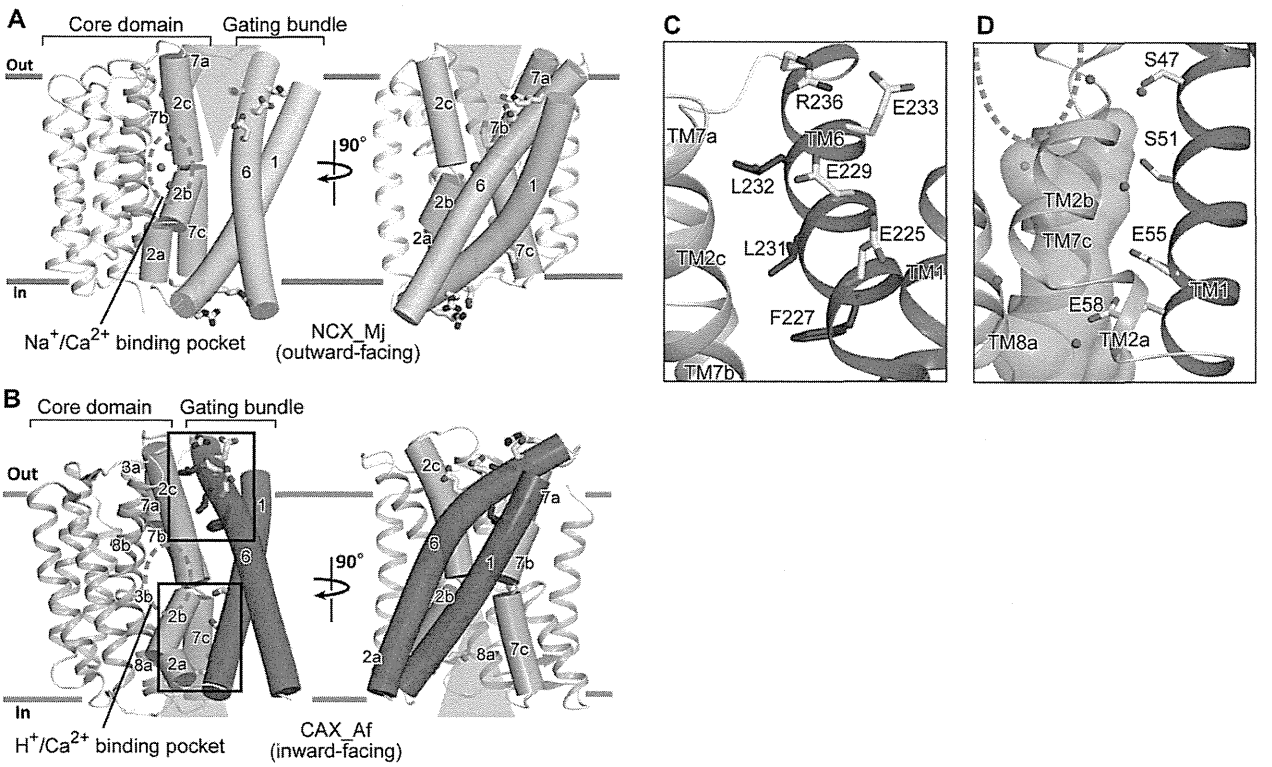

Fig. 2. Structural comparison of CAX_Af and NCX_Mj. (**A** and **B**) Structures of NCX_Mj (A) and CAX_Af (Mol A) (B). The common structures (TM1-10) are shown by coils. TM1, 2, 6 and 7 are shown as cylinders. The cation/Ca^{2+} binding pocket is indicated by a green dotted circle. The ion permeation pathway is indicated by a light-green triangle. The hydrophilic and hydrophobic residues are depicted by yellow and purple stick models, respectively. (**C** and **D**) The extracellular (C) and intracellular (D) sides of the H^+/Ca^{2+} binding pocket in CAX_Af. The cytoplasmic ion permeation pathway was identified with the program CAVER (*13*). Water molecules are represented by red spheres.

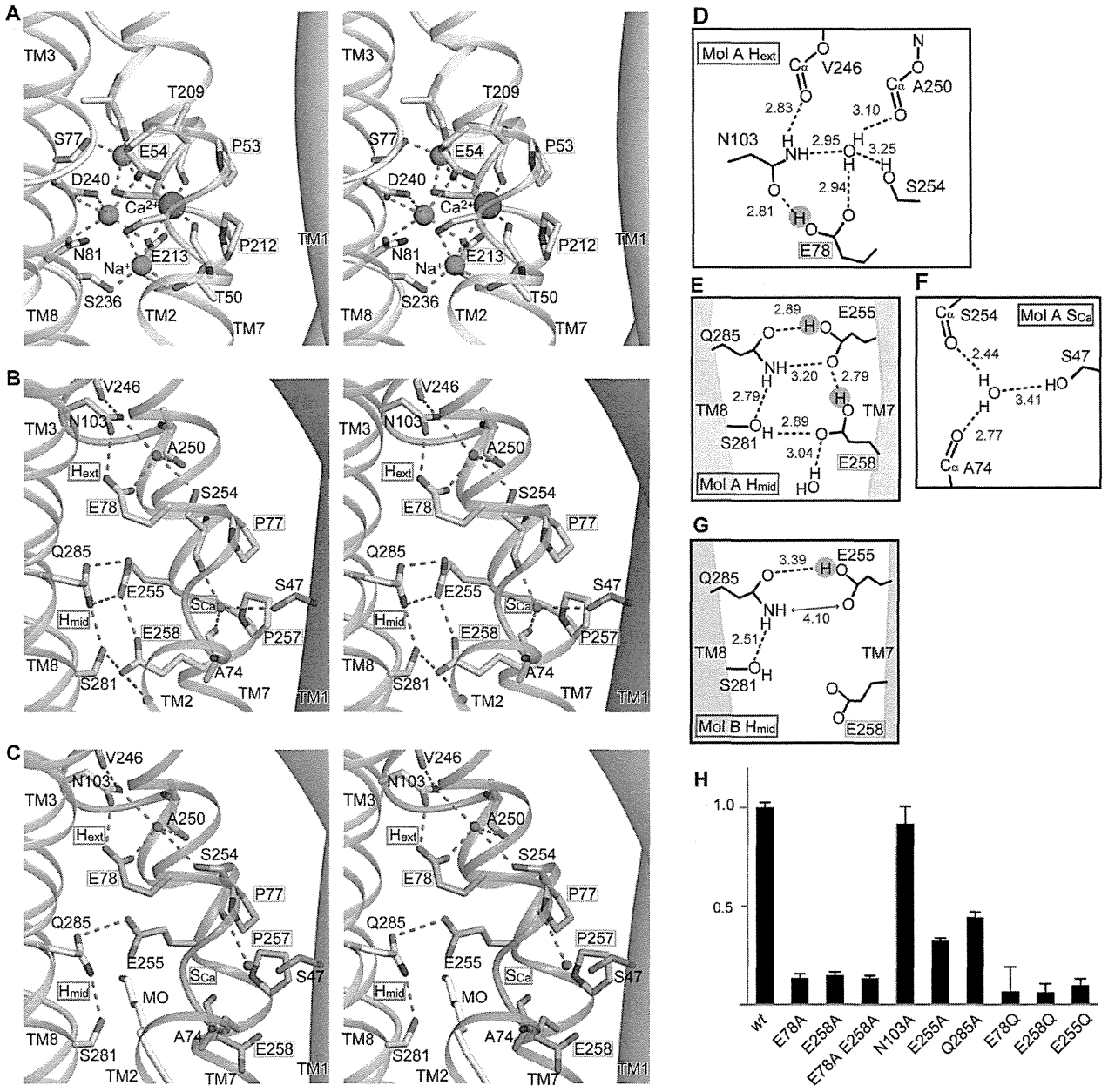

Fig. 3. Cation binding pocket. (**A** to **C**) Stereo views of the Na^+/Ca^{2+} binding pocket in NCX_Mj (A) and the H^+/Ca^{2+} binding pocket in CAX_Af (B: Mol A, C: Mol B). The signature motifs in the α-repeats are highlighted by orange rectangles. In panel (A), The bound Na^+ and Ca^{2+} ions are depicted by green and red spheres, respectively. In panel (B) and (C), Coordinated water molecules are shown by red spheres. The hydrogen-bond networks, H_{ext} and H_{mid}, and the putative Ca^{2+} binding site, S_{Ca}, are indicated. D-G, Schematic drawings of the hydrogen bond geometry in the H^+/Ca^{2+} binding pocket (D-F: Mol A, G: Mol B). H, Liposome-based $^{45}Ca^{2+}$ uptake assays of mutants.

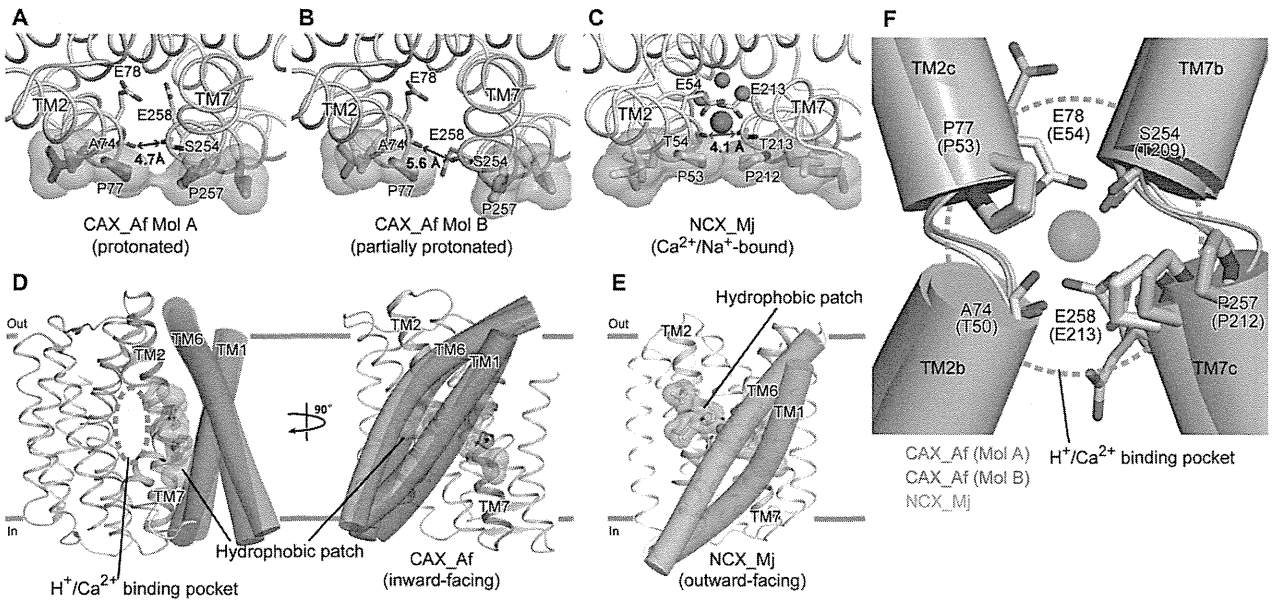

Fig. 4. Hydrophobic patch. (**A** to **C**) Hydrophobic patches of CAX_Af Mol A (A), Mol B (B), and NCX_Mj (C) are shown by green surface-rendered CPK models. D-E, Structural comparison of CAX_Af (D; MolA in blue, MolB in magenta) and NCX_Mj (E). The hydrophobic patches and gating bundles are highlighted. F, Structural comparison of TM2 and TM7 in CAX_Af Mol A (blue), Mol B (magenta), and NCX_Mj (yellow). The residues of NCX_Mj are represented in parentheses.

PLOS ONE

Post-Transcriptional Regulator Hfq Binds Catalase HPII: Crystal Structure of the Complex

Koji Yonekura[1]*, Masahiro Watanabe[1¤], Yuko Kageyama[1], Kunio Hirata[3], Masaki Yamamoto[3], Saori Maki-Yonekura[2]

1 Biostructural Mechanism Laboratory, RIKEN SPring-8 Center, Harima Institute, Sayo, Hyogo, Japan, **2** Bio-Specimen Platform Group, RIKEN SPring-8 Center, Harima Institute, Sayo, Hyogo, Japan, **3** Research Infrastructure Group, RIKEN SPring-8 Center, Harima Institute, Sayo, Hyogo, Japan

Abstract

We report a crystal structure of Hfq and catalase HPII from *Escherichia coli*. The post-transcriptional regulator Hfq plays a key role in the survival of bacteria under stress. A small non-coding RNA (sRNA) DsrA is required for translation of the stationary phase sigma factor RpoS, which is the central regulator of the general stress response. Hfq facilitates efficient translation of *rpoS* mRNA, which encodes RpoS. Hfq helps in the function of other specific proteins involved in RNA processing, indicating its versatility in the cell. However, structural information regarding its interactions with partners is missing. Here we obtained crystals of Hfq and HPII complexes from cell lysates following attempts to overexpress a foreign membrane protein. HPII is one of two catalases in *E. coli* and its mRNA is transcribed by an RNA polymerase holoenzyme containing RpoS, which in turn is under positive control of small non-coding RNAs and of the RNA chaperone Hfq. This sigma factor is known to have a pronounced effect on the expression of HPII. The crystal structure reveals that a Hfq hexamer binds each subunit of a HPII tetramer. Each subunit of the Hfq hexamer exhibits a unique binding mode with HPII. The hexamer of Hfq interacts via its distal surface. The proximal and distal surfaces are known to specifically bind different sRNAs, and binding of HPII could affect Hfq function. Hfq-HPII complexation has no effect on catalase HPII activity.

Citation: Yonekura K, Watanabe M, Kageyama Y, Hirata K, Yamamoto M, et al. (2013) Post-Transcriptional Regulator Hfq Binds Catalase HPII: Crystal Structure of the Complex. PLoS ONE 8(11): e78216. doi:10.1371/journal.pone.0078216

Editor: Dipankar Chatterji, Indian Institute of Science, India

Received July 21, 2013; **Accepted** September 18, 2013; **Published** November 6, 2013

Funding: Funding provided by Grant-in-aid No. 20370064 and 24657111 by the Ministry of Education, Culture, Sports, Science and Technology of JAPAN. The funders had no role in study design, data collection and analysis, decision to publish, or preparation of the manuscript.

Competing Interests: The authors have declared that no competing interests exist.

* E-mail: yone@spring8.or.jp

¤ Current address: Biomass Refinery Research Center, AIST, Higashi-hiroshima, Hiroshima, Japan

Introduction

It is critically important for bacteria to survive environmental changes such as oxidative stress, heat/cold shock, iron excess, phosphosugar toxicity, and UV irradiation. The post-transcriptional regulator Hfq plays a key role in how bacteria cope with stress [1,2] as well as in how hosts react to virulent pathogenic bacteria [3]. Hfq is a member of the family of Sm/Lsm proteins, which is widely distributed in both prokaryotes and eukaryotes. Eukaryotic Sm/Lsm proteins form heteroheptamers, and are involved in mRNA splicing and decay [4–6]. The bacterial Hfq family ranges in length from 70 to 110 amino acid residues and the proteins form thermostable homohexamers [2,7,8]. Hfq is abundant in *Escherichia coli*, with an estimated ~10,000 copies of hexamers per cell [9]. The structures of all Hfq proteins are characterized by an N-terminal α-helix followed by a bent β-sheet composed of five anti-parallel strands and a flexible C-terminal segment [10–15]. The core structure without the C-terminal segment has the topology β5α1β1β2β3β4 and forms the hexamer primarily through intermolecular interactions between strands β4 and β5 of the neighbor. The hexameric toroid with an outer diameter of ~70 Å and a thickness of ~30 Å has two distinct faces [11,12,14,15]. One side of the hexamer is named the proximal side and has a concave surface with radially projecting N-terminal α-helices, while the opposite distal side is convex and consists of β-sheets [11,12,14,15].

Hfq helps small non-coding RNAs (sRNAs) base pair with their target mRNAs and regulate gene translation [2,8,16]. One of the best-studied examples is the post-transcriptional regulation of the stationary phase sigma factor σ^S (RpoS) [17], which is the central regulator of the general stress response in the stationary phase [18]. RpoS recognizes particular promoter sequences in DNA for gene transcription in this phase.

A sRNA, DsrA, consisting of 87 nucleotides, aids in translation initiation of rpoS mRNA [19,20]. At low temperature the rpoS mRNA forms an intramolecular secondary structure that impedes translation initiation. DsrA anneals with rpoS mRNA sequences opposite of the ribosome binding site (RBS), which assists in maintaining the RBS in an open conformation and thus supports translation. Hfq facilitates this process by functioning as an RNA chaperone [17,21].

The stationary phase sigma factor was initially identified as a factor that affects catalase activity in *E. coli*, and its gene was named *katF* [22]. Later, *katF* was found to encode a sigma factor, now recognized as RpoS, which regulates the transcription of the *katE* gene that encodes catalase HPII [23]. HPII is one of two catalases in *E. coli* and is expressed in the stationary phase [24]. RNA polymerase holoenzyme with RpoS transcribes *katE* mRNA

as well as the mRNA of other stress-response proteins. This allows bacteria to survive under oxidative stress in the stationary phase.

Hfq is also involved in termination and destruction of mRNAs [2,8,16,25]. Several studies have indicated that Hfq interacts with components of the ribosome, the RNA-decay machinery and/or other unknown proteins [2,8], but structural information of interactions with other proteins is missing. Here, we report a crystal structure of Hfq and catalase HPII,both endogenous proteins of *E. coli*. The structure reveals that one Hfq hexamer binds each subunit of the HPII tetramer. Further, each subunit of the Hfq hexamer binds uniquely to HPII. Many of the residues on the distal face that interact with HPII are also known to interact with sRNA fragments.

Results and Discussion

Characterization of the crystal

Preparations containing Hfq and catalase HPII were obtained following attempts to express mutant proteins of a Vibrio flagellar motor protein PomAB [26,27]. Cell lysates were processed and subjected to nickel-affinity and gel filtration to yield a concentrated protein solution of Hfq and catalase HPII. We obtained Hfq and HPII only from the constructs that perturbed cell growth following channel induction and overnight incubation. The induction probably increased stress, and likely promoted expression of catalase HPII from the *katE* gene through RpoS. Crystallization trials of the sample solution gave pale green crystals with dimensions of 40 – 100 μm (Fig. S1A in File S1); the color is typical of purified catalase HPII containing heme [28]. To identify the crystal contents, we performed peptide mass finger printing (PMF) MALDI-TOF analysis. Fig. 1A, lane 3 shows an SDS-PAGE gel of crystals dissolved in SDS buffer solution. From bands cut out of the gel, PMF analysis unambiguously identified two proteins, Hfq and catalase HPII, both of which are endogenous in *E. coli*. All the samples showed remarkably high identity scores for the two proteins and no other candidates were flagged in the SwissProt database by Mascot analysis [29]. Bands 1 and 2 were identified as catalase HPII. The molecular weight of HPII is 84 kDa, and bands 1 and 2 correspond to the dimer and monomer, respectively. The molecular weight of Hfq is 11.2 kDa and bands 3 and 4 are the hexamer and monomer of Hfq, respectively. The Hfq hexamer has a histidine cluster around the central pore, and these histidines presumably allowed complexes of Hfq and HPII to bind to the nickel-affinity resin, and be eluted with imidazole (lane 2 in Fig. 1A).

We assayed the activity of catalase within the crystals. The crystals decomposed hydrogen peroxide (H_2O_2) to H_2O and O_2 as shown by a decrease in absorbance at $\lambda = 240$ nm (Fig. S1B in File S1) [30]. Optical microscopic observation showed that the appearance of the crystals did not change much after the assay.

Electron microscopy

We applied a few μl of the isolated protein solution onto a carbon-coated grid and negatively stained it. Electron microscopy (EM) showed large complexes with ring-like structures (Fig. 1B). The total dimension of the complexes is 150 – 160 Å. The diameter of the ring is 70 – 80 Å, which is consistent with that of the Hfq hexamer. Given the long-axis dimension of the rectangular HPII tetramer of ~150 Å, the larger complexes with the rings are most likely Hfq hexamers bound to one HPII tetramer. We cannot tell the exact number of Hfq hexamers associated in each complex due to the limited resolution of the EM images. This observation also supports the view that complex formation takes place prior to crystallization.

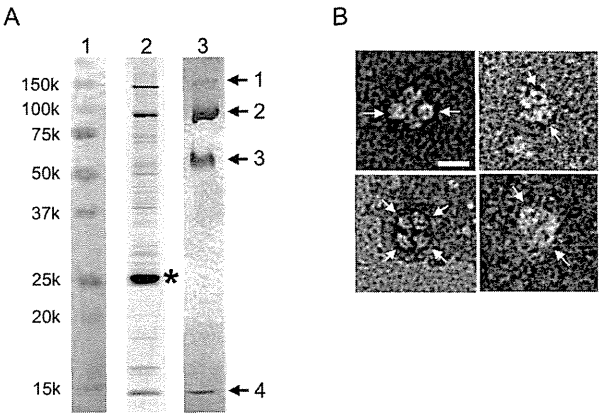

Fig. 1. Characterization of protein samples. (A) An SDS-PAGE pattern of isolated protein solution and crystals of the Hfq and catalase HPII complex dissolved in SDS buffer solution. Lanes are: 1, markers; 2, protein solution after nickel-affinity chromatography; and 3, crystals of Hfq and HPII complex. Arrows and numbers in lane 3 indicate samples for PMF MALDI-TOF analysis. Asterisk in lane 2 indicates an overproduced PomA protein with a histidine tag. Bands 1 and 2 were identified as dimer and monomer of HPII and bands 3 and 4 as hexamer and monomer of Hfq by the PMF analysis, respectively. Note that the fraction eluting from the nickel-affinity column contained significant amounts of both Hfq and HPII. (B) Typical electron micrographs of complexes of endogenous Hfq and HPII prepared with negative staining. Some ring-like structures with dimensions of 70 – 80 Å are indicated with arrows. Bar indicates 100 Å.
doi:10.1371/journal.pone.0078216.g001

Binding of pure Hfq and pure catalase HPII *in vitro*

To determine interactions of Hfq and HPII *in vitro*, we constructed over-expression systems for Hfq and HPII (SI Materials and methods in File S1) and purified them separately. Hfq needed to pass through an anion exchange column to remove bound nucleic acids [31]. Gel-filtration analysis (Fig. S2 in File S1) and dynamic light scattering (DLS; Fig. 2; see below) showed that purified HPII formed tetramers, whereas the Hfq hexameric rings formed dimers in buffer (150 mM NaCl and 20 mM Tris-HCl, pH8.0). Isothermal titration calorimetry (ITC) of injected concentrated Hfq into an HPII solution did not give clear signals of heat changes (SI Materials and methods in File S1). The dimer formation of the Hfq rings is probably through the distal side as in the crystal structure of full-length Hfq [15], the side which is the primary surface for complex formation with catalase HPII (see below). This could explain why ITC did not give clear signals of heat changes at room temperature. After mixing Hfq and HPII and incubating at 4°C overnight, gel filtration showed two separate peaks corresponding to the dimer of the Hfq ring and the HPII tetramer (Fig. S2 in File S1). However, after incubation of Hfq and HPII at 40°C for an hour, the peak fraction of size-exclusion chromatography contained both Hfq and HPII (Fig. S2 in File S1). EM of this fraction resolved complexes with ring-like structures (Fig. S3 in File S1).

DLS showed that the sample solution of Hfq contained one primary species and aggregations or large oligomers (broken line in Fig. 2). The hydrodynamic diameter of this main species is 9.8 nm, which corresponds to a molecular weight of 138 kDa. It is consistent with the dimer of the Hfq hexamer. When Hfq and HPII were mixed and kept at 4°C, DLS gave patterns indicative of aggregates / large oligomers (thin line in Fig. 2). Incubation at 40°C reduced the amount of aggregates and produced complexes with a hydrodynamic diameter of 15.8 nm, which corresponds to

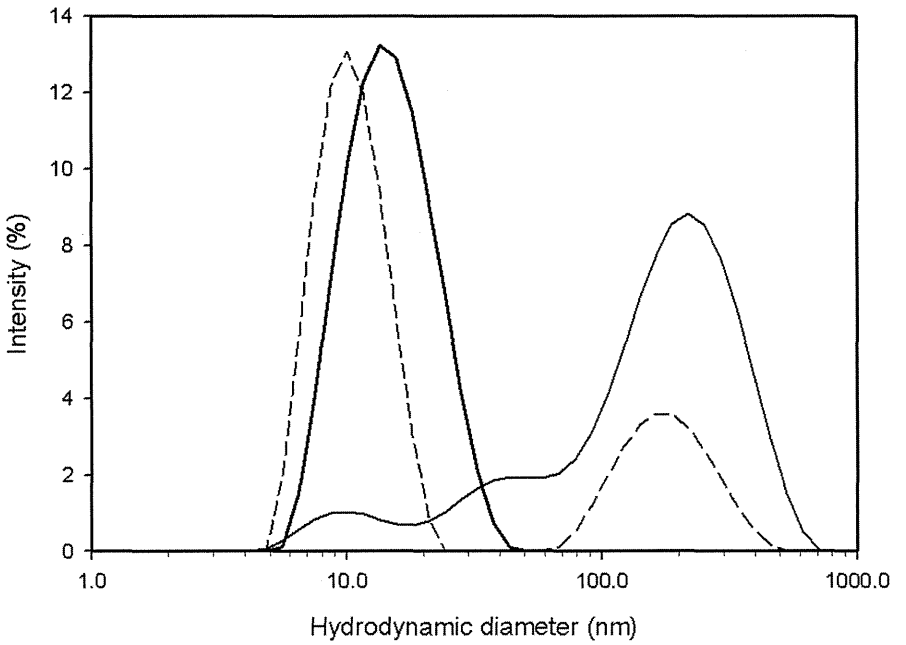

Fig. 2. Intensity profiles of dynamic light scattering (DLS). Broken line: wild-type Hfq (~1.0 mg/ml) after incubation at 40°C. Measured at 25°C. Thin line: mixture of wild-type Hfq (~0.5 mg/ml) and HPII (~0.5 mg/ml) kept at 4°C. Measured at 5°C. Thick line: the same sample as shown in thin line, but after incubation at 40°C. Measured at 25°C. The horizontal axis is common logarithm scale and the vertical axis is percent of the total intensity. The hydrodynamic diameter of the smaller peak in broken line is 9.8 nm corresponding to a molecular weight of 138 kDa, while that of the peak in thick line is 15.8 nm corresponding to ~420 kDa.
doi:10.1371/journal.pone.0078216.g002

a molecular weight of ~420 kDa (thick line in Fig. 2). The peak was broad, suggesting multiple species of complexes (thick line in Fig. 2). Considering the molecular weights of Hfq and HPII, these complexes were probably composed of 1 ~2 Hfq hexamers and one HPII tetramer.

The higher temperature may facilitate dissociation of hexamer dimers, thereby promoting exchange of a Hfq hexameric ring for HPII. However a high temperature does not seem necessary for complex formation in the cell, since we apparently obtained ample formation in our cells grown at 30°C. Hfq-HPII complexes were found in cells stressed by the induction of a foreign membrane protein in an introduced plasmid, which presumably led to the overexpression of HPII. Thus stress and overproduction of HPII may be the physiological cue for complex formation in cells.

Overall structure of the Hfq and HPII complex

Crystals were mounted on a microfocus beam line (BL32XU) at SPring-8 and showed good diffraction of X-rays [32]. We solved the crystal structure at 2.85-Å resolution by molecular replacement with R_{work} and R_{free} values of 19.9% and 24.1%, respectively. Data statistics are shown in Table S1 in File S1. Fig. 3 shows the crystal structure of the complex. Catalase HPII is tetrameric, as in the crystals of pure catalase [33,34], and one Hfq hexameric ring is bound to each corner of the HPII tetramer, one per each individual HPII subunit. The Hfq ring sits on the central core domain of HPII and leans onto a lobe at the C-terminus (Fig. 4A). The core domain of *E. coli* HPII consists of amino acids roughly from 120 to 520 and this domain is conserved from prokaryotes to mammals, whereas the C-terminal lobe consisting of amino acids from roughly 595 to the C-terminal end is variable between species, and bovine catalase has no such C-terminal domain [33].

Approximately 40 residues at the C-terminus of Hfq were missing in the electron density map. This is a common feature in the crystal structure of pure Hfq [15], and consequently the C-terminal region is considered flexible and disordered [11,15]. Formation of the complex does not change the conformations of the HPII tetramer nor the Hfq hexamer. The root-mean-square deviation (RMSD) of Cαs in the Hfq hexamer is ~0.59 Å (total 377 residues in the hexamer) and that in the HPII tetramer is ~0.28 Å from the starting models [15,34].

The packing in the crystal is shown in Fig. 3A. There are no direct contacts between different HPII tetramers nor between different Hfq hexamers. All the contacts are restricted to the interface between Hfq and HPII. To clarify the interactions, we cut out two HPII molecules from adjacent tetramers and two Hfq hexamers as in Fig. 4A. Most of interactions are formed between the distal surface of the Hfq hexamer and the conserved core domain of HPII. We calculated that the buried solvent-accessible surface area (SASA) between this side of one Hfq ring and one HPII molecule is 1066.7 $Å^2$. This value is not large, but would be significant for the complex formation (cf. the buried SASA between a diagonal pair of two HPII molecules in the HPII tetramer is 2014.7 $Å^2$). The Hfq ring structure fits well onto the concave surface of HPII (Fig. 4A). H_2O_2 enters HPII from the lateral side of the molecule, binding to heme at the center of HPII [33]. The Hfq hexamer attached on HPII does not sterically hinder this path (Figs. 3 and 4A) [33]. Thus, the association of the Hfq hexamer with HPII does not interfere with the measured catalase activity (Fig. S1B in File S1).

In contrast, clear contacts on the proximal side of Hfq are limited. We only found a few interactions between N-terminal residues in one Hfq subunit and the lower part of the C-terminal lobe of a neighboring HPII tetramer (Fig. 4A), and categorized

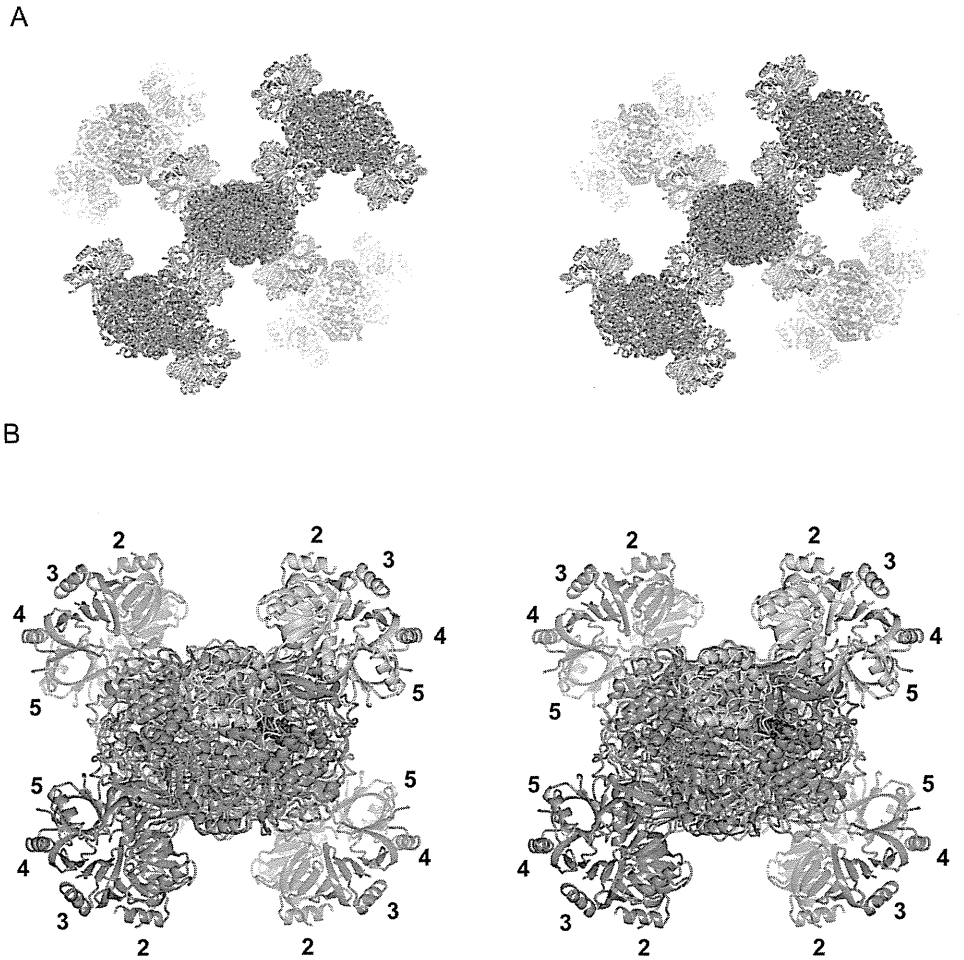

Fig. 3. Crystal structure of the Hfq and catalase HPII complex. (A) Stereo diagram showing the crystal packing of the complex composed of Hfq hexamers in cyan and HPII tetramers in violet. All the four bound Hfq hexamers are displayed for the HPII tetramer at the center, whereas only two hexamers are displayed for each surrounding HPII tetramer for clarity. (B) Structure of one HPII tetramer with four bound Hfq hexamers showing interaction through their distal surfaces. Viewed in stereo. Subunits of one Hfq hexamer are displayed in cyan and green. Numbers 2 – 5 indicate the subunit number in the Hfq hexamer as in Fig. 4. One molecule of the HPII tetramer is displayed in tan (the C-terminal lobe) and in magenta (the other parts). A space-filling model in blue represents heme. Other models are in grey.
doi:10.1371/journal.pone.0078216.g003

these interactions as crystal contacts. This part of the C-terminal lobe is opposite to the surface that interacts with the distal surface of Hfq (Fig. 4A). The flexible C-terminal domain of Hfq may contribute to crystal contacts as presumed from the crystal packing of full-length Hfq [15].

Interactions between Hfq and HPII

Interactions between each Hfq subunit and HPII are unique. To describe the details of the interactions we numbered each Hfq subunit 1 – 6 as in Fig 4B. Subunit 1 is defined as the closest to the C-terminal lobe of HPII. When viewed from the distal side, subunits 2 – 6 were assigned anticlockwise (Fig. 4B). Each subunit has contacts with HPII except for subunit 3, which does not interact with HPII. Between the distal surface of Hfq and HPII, we found that residues for RNA binding [12,14] make interactions with HPII. Those are Gly 29 in Hfq subunit 2 - Asn 157 in the HPII core domain; Gly 29 (subunit 6) - Arg 369 (the HPII core domain); Lys 31 (subunit 2) - Asn 157 (the core domain); Lys 31 (subunit 6) - Pro 295 (the core domain); Tyr 25 (subunit 5) - Glu 363 (the core domain); Asn 28 (subunit 5) - Lys 142 (the core domain); and Ile 30 (subunit 6) - Pro 366 (the core domain). Figs. 5 and S4 in File S1 show close-up views of contacts between the distal surface of subunits 2, 5, 6 and the core domain of HPII. The interface between subunit 1 and the C-terminal lobe of HPII is shown in Fig. S5A in File S1.

The distal surface of the Hfq ring binds adenosine (A)-rich RNAs [12]. There is an adenosine-binding pocket called the A site and another pocket for a purine nucleotide, guanosine or adenosine, called the R site [12]. Lys 31, Leu 32, Gln 33 and Gln 52 from β-strands 2 and 4 primarily form the A site [12], while Tyr 25, Asn 28, Gly 29 and Ile 30 are involved in binding of an adenosine in short RNA fragments at the R site [12,14].

On the proximal side, N-terminal residues in subunit 4 exclusively contribute to the interaction with a HPII molecule in a different tetramer (Fig. 4A). Those include Ser 6 - Gly 645 in the C-terminal lobe of a neighboring HPII molecule; Asn 13 - Glu 610 (the C-terminal lobe); and Pro 10 - Asp 644 (the C-terminal lobe). Most of the proximal side of the hexamer faces the solvent (Figs. 3A

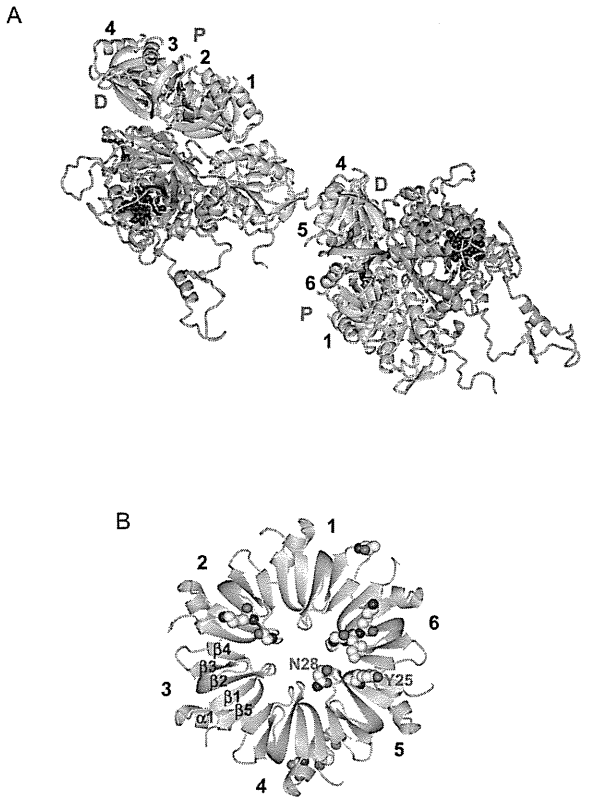

Fig. 4. Some structural details. (A) Two HPII molecules and their interaction partners, two Hfq hexamers. Hfq subunits are color-coded as in Figs. 3B and 4B, and HPII is displayed in tan (the C-terminal lobe) and in violet (the other parts) with heme in blue. "P" and "D" denote the proximal and distal sides of the Hfq hexamer, respectively. (B) Hfq hexamer viewed from the distal side. Residues for binding to HPII are drawn in space-filling representation (see also Table S2 in File S1) with the single-letter amino acid code for Tyr 25 and Asn 28 in subunit 5 (see Fig. 5). Atoms are color-coded as: carbon, yellow; nitrogen, blue; and oxygen, red. "α1" denotes the N-terminal α-helix and "β1" – "β5" β-strands. Numbers 1 - 6 in A and B indicate the subunit number in the Hfq hexamer. Only the Hfq subunits on the front side have the number in A for clarity.
doi:10.1371/journal.pone.0078216.g004

and 4A). Fig. S5B in File S1 shows a close-up view of the interface between the proximal side of subunit 4 and the lower C-terminal lobe of HPII. Table S2 in File S1 has more information on major interactions.

Crystal structures of Hfq with bound RNA reveal that residues around the central pore on the proximal side are responsible for binding of U-rich sRNA segments [10,13,14]. Ser 6, Gln 8 and Asp 9 are involved in a novel uridine-recognition site [14]. Thus complexes of Hfq and HPII could still bind U-rich sRNAs through the exposed proximal side of the Hfq hexamer, as long as the disordered C-terminal domain of Hfq does not occupy this space. The role of the C-terminal domain of Hfq is not clear, but a recent study suggested that this domain also interacts with RNA, which could increase binding specificity [35].

Given that the proximal and distal surfaces of the Hfq ring bind different types of sRNA sequences, complex formation with HPII would limit its repertoire for binding sRNAs in the cell, and

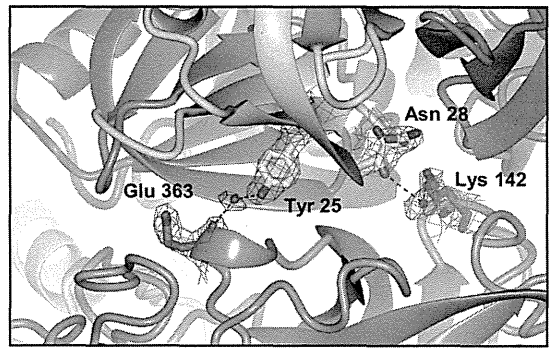

Fig. 5. Interactions between Hfq subunit 5 and HPII. Subunit 5 is displayed in cyan and one molecule of the HPII tetramer is color-coded as in Fig. 4A. Other models are displayed in grey. Interacting residues are drawn in ball-and-stick representation overlaid with 2 Fo - Fc maps of 1.0 σ, and atoms are color-coded as: nitrogen, blue; oxygen, red; and carbon, yellow in Hfq and magenta in HPII. Bonds are depicted as black dashes. Interactions of subunits 2 and 6 with HPII are shown in Fig. S4 in File S1 and those of subunits 1 and 4 are in Fig. S5 in File S1. See also Table S2 in File S1 for bond length and type.
doi:10.1371/journal.pone.0078216.g005

regulate its chaperone function. Further studies are needed to explore this exciting possibility.

Materials and Methods

Samples preparation and crystallization

Complexes of Hfq and catalase HPII were obtained fortuitiously when overexpressing mutants of a bacterial sodium channel protein called PomAB [26,27]. Plasmids containing the corresponding mutant genes fused with a hexahistidine tag sequence were expressed under the control of the T7 promoter. We found that mutants causing a slight disruption to cell growth after induction by IPTG produced a significant amount of the Hfq and catalase HPII complex following overnight incubation at 30°C and isolation by nickel-affinity chromatography. Complexes of Hfq and HPII were found in samples obtained from the cell lysate by nickel-affinity and gel-filtration chromatography and were suspended in 10 mM Tris-HCl (pH 8.0), 50 mM NaCl, 10% (v/v) glycerol, 1 mM DTT and 0.2% (w/v) Cymal5 (Anatrace). Crystals were grown by hanging-drop vapor diffusion at 20°C in a mother liquor containing 0.1 M Tris-HCl (pH 9.0), 0.18 M NaCl and 10% PEG 4000. Pale green crystals grew to 40 – 100 μm over a month (Fig. S1A in File S1). More details are described in SI Materials and methods in File S1.

Protein identification with PMF MALDI-TOF

We collected crystals with a nylon loop and washed them with buffer solution. The crystals were dissolved in SDS sample buffer, heated at ~95°C for 5 min, and then run on a 12.5% homogeneous polyacrylamide gel. Bands cut out from the gel stained with Coomassie brilliant blue were digested with trypsin. The digestion mixtures were subjected to MALDI-TOF MS on an Ultraflex mass spectrometer (Bruker Daltonics) followed by PMF analysis. The obtained MS spectra were used to search the SwissProt 57.15 database using the Mascot program [29], which identified two proteins, Hfq and catalase HPII, and no others.

Electron microscopy

A few μl of the peak fraction of gel filtration was applied onto a carbon-coated copper grid and negatively stained with 2% uranyl

acetate. We examined the sample grids with a JEOL-2100 electron microscope (JEOL) equipped with a LaB_6 gun operated at an accelerating voltage of 200 kV. Images were recorded on a slow-scan charge-coupled device (SSCCD) camera (MegaScan, Gatan) at a final magnification of ~65,000. The magnification was calibrated with negatively stained bovine catalase crystals.

Catalase assay

We selected 5 ~6 crystals from a crystallization plate, washed them with buffer solution, and transferred them into 50 μL of the buffer solution in a 384-well flat-bottom UV-transparent microtiter plate. A 0.5 μL volume of 3% hydrogen peroxide was added to the well of the microtiter plate, and the plate was then immediately scanned in a Varioskan Flash spectrophotometer (Thermo Scientific) [30] at $\lambda = 240$ nm every 1 s for 5 min at room temperature. Catalase decomposes hydrogen peroxide, which has an absorbance peak at $\lambda = 240$ nm, and we measured the decrease in absorbance for an indication of catalase activity.

In vitro binding assay of Hfq and HPII

We cloned the catalase *HPII* and Hfq genes from *E. coli* chromosome, and constructed *Hfq* mutants (SI Materials and methods in File S1). The target proteins were purified by nickel-affinity and anion-exchange chromatography (SI Materials and methods in File S1). Isothermal titration calorimetry (ITC) and dynamic light scattering (DLS) of purified Hfq and HPII were done as in SI Materials and methods in File S1. We carried out analytical gel filtration of Hfq, HPII and mixtures of Hfq and HPII on a Superdex 200 5/150 GL column (GE Healthcare).

Data collection and structure refinement

Crystals ware soaked quickly in glycerol solution by increasing the glycerol concentration stepwise up to 30% and flash-frozen in cold nitrogen gas. Diffraction data were collected on a micro-focus beam line BL32XU of SPring-8 at a wavelength of 1 Å [32]. X-ray diffraction from whole crystals showed high diffuse backgrounds and blurred diffraction spots. A focused beam with a dimension of 1.6×10 μm gave excellent patterns. A total of 180° of diffraction frames were collected in 1° oscillations by shifting the sample by 1 μm every 3 frames. The data were processed to 2.85-Å resolution with HKL2000 [36]. The structure was solved by molecular replacement using PHASER [37], starting from an atomic model of an Hfq hexamer (PDB accession code: 3QHS; 15) and a model of a catalase monomer cut out from an atomic-coordinate file (accession code: 1GGE; 34). The crystals belonged to space group I222 (unit cell dimensions of $a = 136.4$ Å, $b = 159.0$ Å and $c = 167.2$ Å) and contained one Hfq hexamer and one HPII monomer in the asymmetric unit. The structure of Hfq - HPII was refined using REFMAC [38], and manually adjusted with COOT [39]. The stereochemical properties of the models were checked with PROCHECK [40] and the validation tools of COOT. The electron density map resolved amino acids 27 – 753 and one heme molecule for catalase HPII, and 6 – 68 (subunit 1; Fig. 4B), 7 – 69 (subunit 2), 5 – 66 (subunit 3), 5 – 67 (subunit 4), 5 – 67 (subunit 5) and 6 – 68 residues (subunit 6) for the Hfq hexamer. The map did not show ~40 residues at the C-terminus of Hfq. In addition, we were able to pick up 29 oxygen atoms of water in the asymmetric unit. All the figures of molecular graphics were created with CCP4MG [41]. Data collection and refinement statistics are shown in Table S1 in File S1. The atomic coordinates and X-ray diffraction data have been deposited in PDB (code 3VU3).

Supporting Information

File S1 Fig. S1, Crystal of the Hfq and catalase HPII complex and catalase activity of crystals. (A) A typical crystal for X-ray diffraction experiments. Bar represents 100 μm. (B) Assay curve for crystals of the Hfq and catalase HPII complex. Decomposition of hydrogen peroxide (H_2O_2) over time shows the decrease in absorbance at $\lambda = 240$ nm. Time = 0 indicates a point just after H_2O_2 was added. Fig. S2, Analytical gel-filtration of Hfq and HPII. (A) Dashed line: wild-type Hfq after incubation at 40°C. Thin line: mixture of wild-type Hfq (~0.5 mg/ml) and HPII (~0.5 mg/ml) at 4°C. Thick line: the same sample as shown in the thin line, but after incubation at 40°C. The peak in the dashed line corresponds to 138 kDa and the earlier eluting peak at ~1.7 ml in thin line corresponds to ~320 kDa as calibrated with soluble globular proteins used as standards. (B) SDS-PAGE patterns of overproduced and purified Hfq and HPII. Lanes are: 1, marker; 2, Hfq; 3, HPII; and 4, the peak fraction of analytical gel-filtration of mixture of Hfq and HPII shown in the thick line in (A). Arrows are: upper, HPII; middle, hexamer of Hfq; and lower, monomer of Hfq. Other bands probably indicate degradation of HPII after incubation at 40°C. Fig. S3, Typical electron micrographs of protein complexes prepared with negative staining of the peak fraction in thick line in Fig. S2. Purified Hfq and HPII were mixed and incubated at 40°C and gel-filtrated. Protein complexes with ring-like structures are similar to complexes of endogenous Hfq and HPII (Fig. 1B). Bar refers to 100 Å. Fig. S4, Interactions of Hfq subunits 2 and 6 with HPII. (A) Subunit 2 in green. (B) Subunit 6 in green. The figures display the interface between the distal surface of Hfq and the core domain of HPII. The representation scheme of molecules is the same as in Fig. 5. See also Table S2 for more information on the interactions. Fig. S5, Interactions of Hfq subunits 1 and 4 with HPII. (A) Interface between the distal surface of Hfq subunit 1 (cyan) and the C-terminal lobe of HPII. (B) Interface between the proximal surface of Hfq subunit 4 (green) and lower part of the C-terminal lobe of HPII in a neighboring tetramer. The representation scheme is the same as in Fig. 5. Densities for the side chains of Glu 610 are not visible at this contour level. Table S1, Data collection and refinement statistics for the *E.coli* Hfq-catalase HPII complex. Table S2, Major interactions between Hfq and catalase HPII. SI Materials and methods.
(PDF)

Acknowledgments

We thank Yoshiaki Kawano (RIKEN RSC), Koichi Hashimoto (RIKEN RSC) for their help in data acquisition on BL32XU of SPring-8 and Go Ueno (RIKEN RSC) for preliminary data check on BL26B of SPring-8, Takehiro Suzuki (RIKEN ASI) and Naoshi Dohmae (RIKEN ASI) for PMF analysis, Michiyo Takehira and Katsuhide Yutani for ITC experiments, Chikashi Toyoshima for helpful comments on crystallization and X-ray crystallography, and David B. McIntosh and Marcus J. Gallagher Jones for critical reading.

Author Contributions

Conceived and designed the experiments: KY SMY. Performed the experiments: KY SMY YK MW. Analyzed the data: KY MW SMY YK. Contributed reagents/materials/analysis tools: KY YK SMY KH MY. Wrote the paper: KY.

References

1. Tsui HC, Leung HC, Winkler ME (1994) Characterization of broadly pleiotropic phenotypes caused by an Hfq insertion mutation in *Escherichia coli* K-12. Mol Microbiol 13: 35–49.
2. Brennan RG, Link TM (2007) Hfq structure, function and ligand binding. Curr Opin Microbiol 10: 125–133.
3. Chao Y, Vogel J (2010) The role of Hfq in bacterial pathogens. Curr Opin Microbiol 13: 24–33.
4. Kambach C, Walke S, Young R, Avis JM, de la Fortelle E, et al. (1999) Crystal structures of two Sm protein complexes and their implications for the assembly of the spliceosomal snRNPs. Cell 96: 375–387.
5. Tharun S, He WH, Mayes AE, Lennertz P, Beggs JD, et al. (2000) Yeast Sm-like proteins function in mRNA decapping and decay. Nature 404: 515–518.
6. Scofield DG, Lynch M (2008) Evolutionary diversification of the Sm family of RNA-associated proteins. Mol Biol Evol 25: 2255–2267.
7. Franze de Fernandez MT, Hayward WS, August JT (1972) Bacterial proteins required for replication of phage Q ribonucleic acid. Purification and properties of host factor I, a ribonucleic acid binding protein. J Biol Chem 247: 824–831.
8. Vogel J, Luisi BF (2011) Hfq and its constellation of RNA. Nat Rev Microbiol 9: 578–589.
9. Vassilieva IM, Garber MB (2002) The regulatory role of the Hfq protein in bacterial cells. Mol Biol 36: 785–791.
10. Schumacher MA, Pearson RF, Moller T, Valentin-Hansen P, Brennan RG (2002) Structures of the pleiotropic translational regulator Hfq and an Hfq–RNA complex: a bacterial Sm-like protein. EMBO J 21: 3546–3556.
11. Sauter C, Basquin J, Suck D (2003) Sm-like proteins in Eubacteria: The crystal structure of the Hfq protein from *Escherichia coli*. Nucleic Acids Res 31: 4091–4098.
12. Link TM, Valentin-Hansen P, Brennan RG (2009) Structure of Escherichia coli Hfq bound to polyriboadenylate RNA. Proc Natl Acad Sci U S A 106: 19286–19291.
13. Sauer E,Weichenrieder O (2011) Structural basis for RNA 39-end recognition by Hfq. Proc Natl Acad Sci U S A 108: 13065–13070.
14. Wang W, Wang L, Zou Y, Zhang J, Gong Q, et al. (2011) Cooperation of *Escherichia coli* Hfq hexamers in DsrA binding. Genes Dev 25: 2106–2117.
15. Beich-Frandsen M, Večerek B, Sjöblom B, Bläsi U, Djinović-Carugo K (2011) Structural analysis of full-length Hfq from *Escherichia coli*. Acta Crystallogr Sect F Struct Biol Cryst Commun 67: 536–540.
16. Jousselin A, Metzinger L, Felden B (2009) On the facultative requirement of the bacterial RNA chaperone, Hfq. Trends Microbiol 17: 399–405.
17. Muffler A, Fischer D, Hengge-Aronis R (1996) The RNA-binding protein HF-I, known as a host factor for phage Qβ RNA replication, is essential for *rpoS* translation in *Escherichia coli*. Genes Dev 10: 1143–1151.
18. Hengge-Aronis R (2002) Signal transduction and regulatory mechanisms involved in control of the σ^S (RpoS) subunit of RNA polymerase. Microbiol Mol Biol Rev 66: 373–395.
19. Lease RA, Cusick ME, Belfort M (1998) Riboregulation in *Escherichia coli*: DsrA RNA acts by RNA: RNA interactions at multiple loci. Proc Natl Acad Sci U S A 95: 12456–12461.
20. Majdalani N, Cunning C, Sledjeski D, Elliott T, Gottesman S (1998) DsrA RNA regulates translation of RpoS message by an anti-antisense mechanism, independent of its action as an antisilencer of transcription. Proc Natl Acad Sci U S A 95: 12462–12467.
21. Lease RA, Woodson SA (2004) Cycling of the Sm-like protein Hfq on the DsrA small regulatory RNA. J Mol Biol 344: 1211–1223.
22. Loewen PC, Triggs BL (1984) Genetic mapping of *katF*, a locus that with *katE* affects the synthesis of a second catalase species in Escherichia coli. J Bacteriol 160: 668–675.
23. Mulvey MR, Loewen PC (1989) Nucleotide sequence of *katF* of *Escherichia coli* suggests KatF protein is a novel a transcription factor. Nucleic Acids Res 17: 9979–9991.
24. Visick JE, Clarke S (1997) RpoS- and OxyR-independent induction of HPI catalase at stationary phase in Escherichia coli and identification of *rpoS* mutations in common laboratory strains. J Bacteriol 179: 4158–4163.
25. Rabhi M, Espéli O, Schwartz A, Cayrol B, Rahmouni AR, et al. (2011) The Sm-like RNA chaperone Hfq mediates transcription antitermination at Rho-dependent terminators. EMBO J 30: 2805–2816.
26. Yonekura K, Yakushi T, Atsumi T, Maki-Yonekura S, Homma M, et al. (2006) Electron cryomicroscopic visualization of PomA/B stator units of the sodium-driven flagellar motor in liposomes. J Mol Biol 357: 73–81.
27. Yonekura K, Maki-Yonekura S, Homma M (2011) Structure of the Flagellar Motor Protein Complex PomAB: Implications for the Torque-Generating Conformation. J Bacteriol 193: 3863–3870.
28. Loewen PC, Switala J (1986) Purification and characterization of catalase HPII from *Escherichia coli*. K12. Biochem. Cell Biol 64: 638–646.
29. Perkins DN, Pappin DJ, Creasy DM, Cottrell JS (1999) Probability-based protein identification by searching sequence databases using mass spectrometry data. Electrophoresis 20: 3551–3567.
30. Li Y, Schellhorn HE (2007) Rapid kinetic microassay for catalase activity. J Biomol Tech 18: 185–187.
31. Beich-Frandsen M, Večerek B, Konarev PV, Sjöblom B, Kloiber K, et al. (2011) Structural insights into the dynamics and function of the C-terminus of the *E. coli* RNA chaperone Hfq. Nucleic Acids Res 39: 4900–4915.
32. Hirata K, Ueno G, Nisawa A, Kawano Y, Hikima T, et al. (2010) New micro-beam beamline at SPring-8, targeting at protein micro-crystallography. AIP Conf Proc 1234: 901–904.
33. Bravo J, Mate MJ, Schneider T, Switala J, Wilson K, et al. (1999) Structure of catalase HPII from *Escherichia coli* at 1.9 Å resolution. Proteins 34: 155–166.
34. Melik-Adamyan W, Bravo J, Carpena X, Switala J, Maté MJ, et al. (2001) Substrate flow in catalases deduced from the crystal structures of active site variants of HPII from *Escherichia coli*. Proteins 44: 270–281.
35. Vincent HA, Henderson CA, Ragan TJ, Garza-Garcia A, Cary PD, et al. (2012) Characterization of *Vibrio cholerae* Hfq provides novel insights into the role of the Hfq C-terminal region. J Mol Biol 420: 56–69.
36. Otwinowski Z, Minor W (1997) Processing of X-ray diffraction data collected in oscillation mode. Methods Enzymol 276: 307–326.
37. McCoy AJ, Grosse-Kunstleve RW, Storoni LC, Read RJ (2005) Likelihood-enhanced fast translation functions. Acta Crystallogr D 61: 458–64.
38. Murshudov GN, Vagin AA, Dodson EJ (1997) Refinement of macromolecular structures by the maximum-likelihood method. Acta Crystallogr D 53: 240–55.
39. Emsley P, Cowtan K (2004) Coot: Model-building tools for molecular graphics. Acta Crystallogr D 60: 2126–2132.
40. Laskowski RA, MacArthur MW, Moss DS, Thornton JM (1993) PROCHECK: A program to check the stereochemical quality of protein structures. J Appl Crystallogr 26: 283–291.
41. McNicholas S, Potterton E, Wilson KS, Noble MEM (2011) Presenting your structures: the CCP4mg molecular-graphics software. Acta Cryst D 67: 386–394.

3D Manipulation of Protein Microcrystals with Optical Tweezers for X-ray Crystallography

Journal of Physics: Conference Series **425** (2013) 012011 doi:10.1088/1742-6596/425/1/012011

3D Manipulation of Protein Microcrystals with Optical Tweezers for X-ray Crystallography

T Hikima[1], K Hashimoto[1], H Murakami[1], G Ueno[1], Y Kawano[1], K Hirata[1], K Hasegawa[1,2], T Kumasaka[1,2] and M Yamamoto[1]

[1] RIKEN SPring-8 Center, Hyogo, 679-5148, Japan
[2] JASRI/SPring-8, Hyogo, 679-5198, Japan

E-mail: yamamoto@riken.jp

Abstract. In some synchrotron facilities such as SPring-8, X-ray microbeams have been utilized for protein crystallography, allowing users to collect diffraction data from a protein microcrystal. Usually, a protein crystal is picked up manually from a crystallization droplet. However it is very difficult to manipulate the protein microcrystals which are very small and fragile against a shock and changes of temperature and solvent condition. We have been developing an automatic system applying the optical tweezers with two lensed fiber probes to manipulate the fragile protein microcrystal. The system succeeded in trapping a crystal and levitating it onto the cryoloop in the solvent. X-ray diffraction measurement for the manipulated protein microcrystals indicated that laser irradiation and trap with 1064nm wavelength hardly affected the result of X-ray structural analysis.

1. Introduction

We have constructed and are operating a micro-focus beamline, BL32XU at SPring-8 with the objective of collecting diffraction data from protein crystals in the micron size range [1]. Users who deal with microcrystals have special difficulties in preparation of frozen samples, namely picking up a microcrystal from the solution with a cryoloop, freezing, and packing it into a cryo-sample container. To reduce the difficulty, we have been developing an automatic system, adopting optical tweezers as a manipulation tool of fragile protein microcrystals. The optical tweezers can manipulate a micron-sized dielectric object without touching that object [2-4]. It was also reported that optical tweezers in the near-infrared region can trap and manipulate a living cell without critical photodamage [5]. We applied optical tweezers composed of two lensed fiber probes [6] to manipulate a protein microcrystal in solution. A schematic drawing of two-lensed fiber probes and the principle by which they can be used to trap a dielectric object are shown in figure 1. The probes of the optical tweezers with the lensed fibers are small enough to be inserted into a crystallization droplet within various crystallization plates and have an advantage for manipulation of the object with lower emission power than with

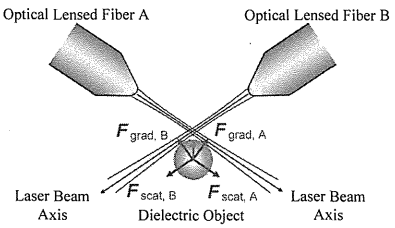

Figure 1. Optical forces acting on a dielectric object. Near the cross-focus point of the laser beams, the scattering force, F_{scat}, and gradient force, F_{grad}, act on the dielectric object. The total force acts on the object as buoyancy (shown by red arrow). The object is captured and held at equilibrium point where the force of gravity and of buoyancy are equal [6].

optical tweezers based on a conventional condensing lens. We evaluated the optical tweezers system with two lensed fiber probes for X-ray protein crystallography.

2. Experimental

The optical tweezers system is composed of two lensed fiber probes attached to two electric *xyz* micro-manipulators M200 (Suruga Seiki Co., Ltd.), an inverted microscope ECLIPSE TE2000-U (Nikon Co., Ltd.), and two Ytterbium Fiber Laser module YLM-1-1064 (IPG Laser GmbH) with an emission wavelength of 1064nm. Each laser module is connected to each lensed fiber probe. A single-mode tapered lensed fiber for NSOM probe (Nanonics Imaging Ltd.) is applied to the probe of the optical tweezers. The numerical aperture of the probe is 0.22 and the spot diameter is 5μm in the theoretical specification. Photographs of the system are shown in figure 2. A cryoloop attached on the top of a manual micro-manipulator is inserted into the crystallization droplet. The optical tweezers pick up and put a microcrystal into the cryoloop in the droplet. The droplet is cooled at 20℃ by the temperature-controllable cooling plate to avoid vaporization. The emission power at the sample position is calibrated using a laser power meter OPM-370 (Sanwa Electric Instrument Co., Ltd.).

In addition, we set up another optical tweezers system with a large condensing lens as a probe to investigate the tolerance of protein crystals to high power irradiation from a near-infrared laser. The large condensing system could not levitate a protein crystal in the solution, but could move it horizontally and irradiate the sample with near-infrared laser light of emission power up to 760mW.

Two protein crystal sample types were prepared in this study. Microcrystals of lysozyme were for 3D manipulation by the optical tweezers with two lensed fibers and rod-like crystals of thermolysin were for the investigation of irradiation tolerance. After manipulation by the optical tweezers, the crystals were pulled out from the crystallization drop together with cryo-protectant and were rapidly frozen in liquid nitrogen. X-ray diffraction data for the lysozyme and thermolysin crystals were collected at BL41XU [7] and BL45XU [8] at SPring-8, respectively. Data collection protocols, such as the total X-ray dose and oscillation region, were optimized to minimise X-ray radiation damage to the crystals. The diffraction images were processed using HKL2000 [9]. Initial phase was derivered by molecular replacement. The molecular structures were refined using the program CNS [10].

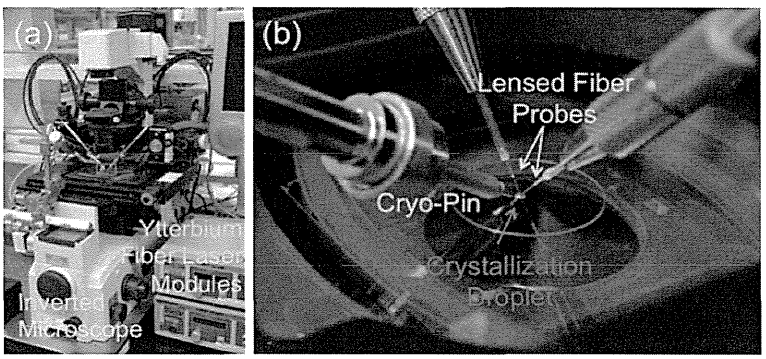

Figure 2. Photographs of the optical tweezers system with two lensed fiber probes: (a) Overall view. (b) Enlargement around a crystallization droplet with the volume of ca. 10μ*l*, enclosed in red box in (a). Protein microcrystals in the droplet are observed from the bottom by the inverted microscope.

3. Results and discussion

The optical tweezers with two lensed fiber probes succeeded in trapping protein crystals with sizes between 5 to 30μm and manipulating them in the horizontal and vertical directions. Crystals over 30μm in size could not be levitated by the optical tweezers. The emission power to manipulate the crystals is less than 10mW per probe at the sample position, which is remarkably smaller than the few hundred milliwatts of the optical tweezers with the conventional condensing lens system [11]. The system also succeeded in manipulating a 1μm polystyrene bead. The continuous images captured during the manipulation of a 15μm lysozyme crystal are shown in figure 3. The crystals were soaked in a crystallization droplet including 30% glycerol as cryo-protectant. The crystal on the bottom of the drop was trapped by the optical tweezers, as shown in figure 3(a), and then levitated and moved onto a

cryo-mount loop, LithoLoops™, with 0.02mmϕ, as shown in figures 3(b)-(d). The crystal was released over the loop and allowed to sink down into the loop, as shown in figure 3(e). Just after the crystal caught in the loop, the loop was pulled out from the droplet, as shown in figure 3(f). Manipulation by the optical manipulation was complete within 30sec. After the manipulation, no damage was observed to the shape of crystals. On the other hand, the loop made of polyimide film was sometimes burned out by irradiation of the focused beam. The statistics of X-ray diffraction data collection for the manipulated lysozyme crystals are shown in table 1. Tweezers 1 and 2 labeled in dataset column indicate the crystals picked-up by the optical tweezers, and manual 1 indicates the crystals picked-up manually as references. Each dataset was collected from different lysozyme crystals. As total X-ray dose in the data collection was limited to less than 0.5MGy, X-ray radiation damage of each crystal would be negligible. There was no significant difference in the statistics of crystals manipulated by the optical tweezers and by hand. In addition, there was no difference in the structure refinement statistics of the datasets (data not shown). In particular, the relative isotropic *B* factor is a key criterion for X-ray radiation damage. On the other hand, there is no criterion to evaluate the photodamage of biomolecules by the near-infrared laser, because the detailed influence of the laser on biomolecules is not clear. A composite omit electron density map generated by CNS suggested that there was no photodamage at amino-acid side chains and disulfide bonds compared to these of the molecular structure without near-infrared laser irradiation. It is indicated that manipulating by the optical tweezers hardly affected the X-ray crystal structure analysis.

Thermolysin crystals which were used in the investigation of the tolerance of protein crystals to high irradiation from a 1064nm laser were rod-like crystals with the longest dimension ~ 300μm. The crystals were soaked in cryo-protectant solution including 30% PEG400. One of two edges of a crystal was trapped by the optical tweezers with high emission power of 760mW for 60sec at room temperature. Two X-ray diffraction datasets were collected for a single crystal at both edges with and without irradiation of the laser, respectively. The total X-ray dose in the data collection was restricted to less than 5MGy. The statistics of X-ray analysis are shown in table 1. Datasets of trap1, free1 and trap2, free2 were collected from the same crystal, respectively. There was no significant difference in the statistics between the datasets with and without irradiation by the high power laser. R.m.s. deviations between the molecular structures in the single crystal are smaller than 0.04Å, indicating that the laser irradiation hardly affected the molecular structure. It was reported that aerobic conditions increased the photodamage of living cells by a near-infrared laser compared to anaerobic conditions

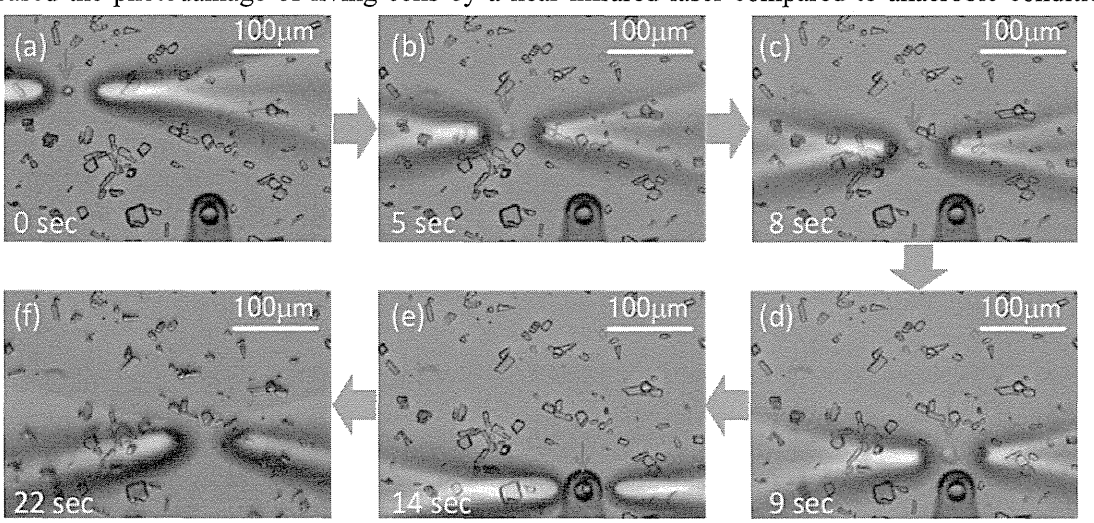

Figure 3. Lysozyme crystal (indicated by red arrow) was trapped by the optical tweezers and levitated onto a cryo-mount loop in (a) - (g). The time displayed at left-down in each frame shows an elapsed time after trapping the crystal. In the last frame (f), the loop which caught the crystal had been pulled out from the droplet.

[5]. However, the result of our structure analysis suggested that there was no influence of oxidative damage in the crystals irradiated with a strong near-infrared laser. Therefore, it was estimated that the irradiation of near-infrared laser with lower emission power hardly affected the molecular structure of proteins.

4. Concluding remarks

Optical tweezers with two lensed fiber probes succeeded in trapping protein crystals smaller than 30μm and levitating them onto the cryoloop in the solvent. X-ray diffraction measurement of the manipulated protein crystals indicated that laser irradiation and trap with 1064 nm wavelength hardly affected the result of X-ray structural analysis. The optical tweezers will be a powerful tool to manipulate a fragile protein microcrystals for X-ray crystallography. Based on the results, we are developing an automatic protein microcrystal pick-up and freezing system combining the optical tweezers with an automatic cryo-sample exchanger, SPACE [12].

This work is supported by the Targeted Proteins Research Program which is a national project promoted by the Ministry of Education, Culture, Sports, Science and Technology (MEXT) of Japan.

Table 1. Crystal size and X-ray diffraction data collection statics.

Crystal sample	Lysozyme			Thermolysin			
Dataset	tweezers1	tweezers2	manual1	trap1	free1	trap2	free2
Crystal size(μm^3)	15x15x20	15x15x10	25x25x25	300x30x30		280x30x30	
Data Collection Statistics							
Resolution (Å)	50–1.70 (1.76–1.70)			50–2.08 (2.15–2.08)			
Space group	$P4_32_12$			$P6_122$			
Cell dimension: *a*, *c* (Å)	79.3, 37.1	79.9, 37.0	79.2, 37.0	92.7, 129.3	92.8, 129.3	92.8, 129.5	92.6, 129.7
R_{sym}[a] (%)	6.1 (31.5)	6.7(37.0)	6.5(33.7)	8.7(15.6)	8.6(14.8)	8.7(15.7)	8.4(16.1)
I / σ	35(7)	23(4)	34(7)	45(18)	46(19)	48(20)	45(16)
Isotropic *B* factor ($Å^2$)	14.1	14.3	15.1	9.1	8.7	8.3	9.4
Mosaicity (°)	0.40–0.43	0.25–0.30	0.23–0.35	0.127	0.100	0.091	0.122

[a] $R_{sym} = \Sigma|I_i - \langle I \rangle| / \Sigma|I_i|$, where I_i is the intensity of an observation and $\langle I \rangle$ is the mean value for that reflection and the summations are overall reflections.

References

[1] Hirata K et al, 2010, *AIP Conf. Proc.*, **1234**, 901-4.
[2] Neuman K C et al, 2004, *Rev. Sci. Instrumentations*, **75(9)**, 2787-809
[3] Constable A et al, 1993, *Optics Lett.*, **18(21)**, 1867-9.
[4] Santucci S C et al, 2011, *Anal. Chem.*, **83(12)**, 4863-70.
[5] Neuman K C et al, 1999, *Biophys. J.*, **77**, 2856-63.
[6] Taguchi K et al, 2000, *Optics Comm.*, **176**, 43-7.
[7] Kawano Y et al, 2010, *AIP Conf. Proc.*, **1234**, 359-62.
[8] Kumasaka T et al, 2002, *Structure*, **10**, 1205-10.
[9] Otwinowski Z and Minor W, 1997, *Methods Enzymol.*, **276**, 307-26.
[10] Brunger A T et al, 1998, *Acta Cryst. D*, **54**, 905-21.
[11] Bancel P A at al, 1999, *J. Cryst. Growth*, **196**, 685-90.
[12] Murakami H et al, 2012, *J. Appl.Cryst.*, **45**, 234-8.

通巻第755号 昭和42年2月6日第三種郵便物認可（毎月1回1日発行） 平成25年1月1日発行

ISSN 0451-2014

化学工業

CHEMICAL INDUSTRY

2013 VOL.64 NO.1 1

■特集／次世代健康・医療・福祉の科学

化学工業社

切らずに治すがん治療薬の開発

石川義弘[*1]・江口晴樹[*2]

1．はじめに

悪性新生物，いわゆる「がん」は，心疾患，脳血管疾患と並び，現在のわが国における3大死亡原因である．悪性新生物による死亡は，平成21年には34万4105人となっている[1]．この数字は前年度に比べて1000人以上の増加であり，人口の高齢化とともに，がんの国民疾患に占める重要性は，ますます増加すると考えられる．がんの種類でいうと，かつて首位を占めていた胃がんが減少傾向にあり，大腸がんや肺がんにとってかわられつつある．特筆すべきは，乳がんや膵がんなど，かつてはさほど多くなかったがんが次第に順位をあげていることである．これも戦後数十年以来の国民の食生活の変化を物語っているのかもしれない．胃がんの死亡者数の減少には，刺激性食物など食生活の変化はもちろんだが，世界でも先駆的なさまざまな診断および治療技術の進歩があったと思われる．胃がんをいかに早期発見するかは消化器内科医の悲願であり，いわゆる二重造影法をはじめとして，その後は胃内視鏡技術がわが国で開発され，世界に誇る技術となっている．内視鏡の製造会社としては，現在でもオリンパスなどの国内メーカーが，世界シェアの大半を占めている．消化管のがんに対しては内視鏡的手術の進歩とともに，胃がん撲滅への挑戦が続けられている．近年では放射線療法においても，がん治療技術の革新が目覚ましく，重粒子線や陽子線治療などが成果を上げている．しかるに内視鏡などの簡便な装置に比べると，放射能設備を備えた大型治療装置が必要であり，建設費用も数十億円以上かかるなど，必ずしも簡便な治療法ではない．

そこで本原稿では，内視鏡ほど簡便ではないが，重粒子線ほど複雑ではない，がんの治療法として温熱療法をまとめてみたい．とりわけ近年EU諸国で実用化された，マグフォース社による超局所選択的な温熱療法について紹介するが，さらにこの治療法を凌駕するわが国のがん治療についても知見をまとめる．現在われわれが開発を進めているのが，IHIの持つ造船技術を医薬品開発に応用したものである．いわゆる一般医薬品中から，これまで解析の対象となっていない物理的な特性を検討する手法である．創薬のツールとして，あるいは磁性を有する化合物を選んだり設計する手法であり，有機磁性体開発の新技術である．造船技術における材料開発手法の医療転用であり，今後の新薬のスクリーニングや抗がん剤など新規医薬品化合物の開発に強力な武器となると考えられる．

2．最近の抗がん治療技術の進歩

2．1　温熱療法について

がん細胞では代謝が亢進しており，いわゆる代謝に伴う活性酸素などの産生も多いことが知られている．これはがん細胞の盛んな分裂能を示していると思われる．一般に細胞は温度の上昇に伴って，酵素活性の上昇とともに代謝活性が上がることが知られている．よく知られている体温の36.5度で，われわれの体の酵素活性が最大となるので

[*1] Yoshihiro Ishikawa　横浜市立大学大学院医学研究科　循環制御医学　教授　医学博士
[*2] Haruki Eguchi　㈱IHI　技術開発本部基盤技術研究所応用理学研究部　主幹研究員　工学博士
How to treat cancer without surgery?

はなく，更に高い温度まで酵素活性が上昇する．例えば細胞内セカンドメッセンジャーを産生するアデニル酸シクラーゼは，すべての細胞に発現する基本的な細胞酵素であるが，その酵素活性は37度で最大を示すのではなく，42度まで温度依存性に上昇していく．一見すると温度が上がって酵素活性が上がることはよさそうだが，アデニル酸シクラーゼの場合でも高温化で長時間さらされると，やがて酵素活性が低下し，失活することが知られている．いったん高温にさらされて失活した酵素が，再び酵素活性を取り戻すことはない．おそらく酵素蛋白の立体構造の変化を伴って不可逆的な失活を起こしていると考えられる．

そこで，もともと代謝活性の高いがん細胞が，高温にさらされれば代謝活性はさらに上昇し，これが長く続けばがん細胞に対して殺傷効果を持つのではないかということが容易に推測できる．歴史的にも，高熱疾患にかかった患者の腫瘍が縮小したことが報告されており，がんの自然治癒症例においては発熱が何らかの原因であったという報告もある．さらに温熱によって免疫能力が高まることがさまざまな実験からも明らかとなっており，がんに対する免疫能力の亢進から，がん細胞に対する治療効果が表れるとも考えられている．このような事実から，がん組織を高熱にさらすことによって，抗がん治療を行おうという発想が生まれた．本格的な研究が始まったのは60年代以降であるが，さまざまな治療温熱装置が考案されており，治療成果を上げている．一般にはがん組織の温度が41度以上になるとがん細胞に対して殺傷効果が見られ，42.5度で理想的な殺傷効果を来すとされているが，がん細胞種にもより，温熱に対して感受性の高いがんもあれば，さほど高い感受性を示さないものもある．

2．2　全身と局所温熱について

がん細胞のみを標的にした温熱療法であるならば，がん組織の温度だけを選択的にあげればよい．周りの健常細胞も，温熱によってダメージが皆無というわけではないから，がん組織選択的な温熱療法が理想である．しかしながら，局所的な温熱療法は，物理的な手法の制限から困難である．皮膚などの体表にある病変組織であれば，局所に対して物理的なプローベを用いて温熱を付加することが容易である．しかるに深部臓器に対して臓器選択的に温熱を付加することが難しい．そこでわが国で開発されたのが，サーモトロンをはじめとする温熱治療器である．これは相対向する2枚の電極で体をはさみ，高周波エネルギーを利用してがん組織に対して加温を行い，がん殺傷効果を引き起こすものである．対抗する電極の大小の組合せや，出力の調節により，浅部から深部がんに及ぶまで温熱作用を示すことができるため，全国の施設で使用されている．しかしながら，治療効果としては必ずしも他の方法に勝っているともいえず，単独療法として行われるのではなく，他の治療法の補助療法として，あるいは緩和を目的として施行されることも多い．加温だけであるために副作用がほとんどなく，この点においては末期がんや治療困難な症例に対しても有意義と考えられる．

2．3　選択的局所温熱について

磁性鉄粒子を利用して，交流磁場印加によってそのヒステリシス特性を利用して発熱させる手法が，わが国でも盛んに研究されてきた．かつての磁性鉄粒子を直接使用した手法から，近年ではリポソームに包埋したり，表面にナノコーティングを施し，組織親和性を高めたさまざまな磁性粒子が使用されている．しかるに本邦では実用化に至るまでにさまざまな困難があり，実際の治療で汎用されるに至っていない．これに対して近年欧州で開発されたのが，磁性鉄粒子を用いた超選択的な温熱療法である．マグフォース社によって開発されたNanoActivatorという交流磁場印加装置と，NanoTermという名で販売されている酸化鉄粒子の組合せによりEUにおける認可を受けている．現在のところ適応疾患としては，神経膠芽腫のみであるが，すでにEU 27ヵ国で承認を受けており，現在EU域内では画期的な局所温熱療法として注目を集めている．治療の原理はいたって簡単で，頭蓋内の神経膠芽腫の部分に特殊コーティングを施された酸化鉄粒子を局所注入し，頭蓋を覆うように配置した交流磁場印加装置で腫瘍組織を選択的に加温するものである．発熱体として磁性鉄を使用しているために，局所が極めて高熱化し，